NULL-SPACING PREPROCESSING FOR UAV CLASSIFICATION FROM RF IQ SIGNALS UNDER ISM-BAND INTERFERENCE

NGUYEN DANG HIEU[1,2]*, NGUYEN LE CUONG[2], TRAN VU KIEN[2]
[1] *Faculty of Electronics, Telecommunications and Professional Engineering – Academy of Security Engineering and Technology*
[2] *Electric Power University*
** Corresponding author: hieund@hvktcnan.edu.vn*
DOIs: https://www.doi.org/ 10.46242/jstiuh.v83i5. 6187

Abstract. Unmanned aerial vehicle (UAV) classification from radio-frequency (RF) in-phase/quadrature (IQ) signals in industrial, scientific, and medical (ISM) bands is often degraded by background noise and co-channel interference. This paper investigates Null-Spacing as an IQ-domain preprocessing step that attenuates structured interference before short-time Fourier transform (STFT) or continuous wavelet transform (CWT) representation. The interference subspace is estimated from Wi-Fi/Bluetooth samples in the training set, and each IQ signal is projected onto its orthogonal complement. The method is evaluated on the CardRF dataset with five UAV classes under additive white Gaussian noise (AWGN), Wi-Fi, Bluetooth, mixed interference, and jointly negative signal-to-noise ratio (SNR) and signal-to-interference ratio (SIR) conditions. With the STFT + convolutional neural network (CNN) configuration at $\eta = 0.99$, Null-Spacing improves macro-F1 from 82.82% to 84.56% and accuracy from 82.95% to 84.61%. Under negative-SNR AWGN, macro-F1 increases by 9.165 percentage points. Control experiments further show that the gain does not come from arbitrary projection alone, but from an interference subspace derived from Wi-Fi/Bluetooth references. The results support Null-Spacing as a conditional preprocessing step: it improves robustness under several difficult noisy and interfered conditions, but is not uniformly beneficial across all signal conditions.
Keywords: CWT, interference subspace, ISM band, null-spacing, orthogonal projection, RF IQ signal, STFT, structured interference, UAV classification.

1. INTRODUCTION

The growing use of small UAVs in civilian, industrial, and commercial applications increases the need for passive RF monitoring and early detection of UAV emissions. Compared with optical, radar, and acoustic sensors, passive RF sensing can exploit emissions already produced by UAV systems and is less dependent on lighting conditions [1-3]. In this approach, an RF IQ signal is a down-converted baseband signal represented by in-phase and quadrature components. The received signal may contain UAV emissions, controller signals, and emissions from other transmitters operating in the same band.

In ISM bands, UAV signals often coexist with Wi-Fi, Bluetooth, and other RF sources. These sources produce structured interference that may overlap with UAV signals in time, frequency, or both. When the SNR or SIR is below 0 dB, discriminative UAV components may be masked, and the classifier may learn noise- or interference-dominated features [3].

CardRF is used in this study because it contains UAV, Wi-Fi, and Bluetooth signals collected in the 2.4 GHz band [4]. This structure fits the purpose of the paper: Wi-Fi/Bluetooth samples are used to estimate an interference subspace, and the effect of projection on UAV classification is then evaluated. Recent datasets such as RFUAV and CageDroneRF also show a trend toward larger and more diverse RF-UAV benchmarks [5, 6], but CardRF is selected here because it provides the reference Wi-Fi/Bluetooth signals needed for the proposed preprocessing.

Previous studies have used RF fingerprints, wavelet features, spectrograms, CNNs, residual networks (ResNets), and hierarchical models for RF-based UAV classification [2, 3, 7-15]. Some studies also consider low-SNR or interference conditions [10, 12, 14, 15]. However, most pipelines transform the RF IQ signal into a feature or spectrogram before classification. If Wi-Fi/Bluetooth components are already present in the IQ signal, they may still appear in the STFT or CWT representation. This motivates an IQ-domain preprocessing step before representation formation.

From a signal-processing perspective, structured interference may concentrate energy along a

© 2026 Industrial University of Ho Chi Minh City

limited number of dominant directions. Prior work on subspace models and orthogonal projection shows that projecting an observation onto the orthogonal complement of an interference subspace can attenuate unwanted components [16-20]. Motivated by this idea, this paper investigates Null-Spacing as an IQ-domain preprocessing step. The interference subspace is estimated from Wi-Fi/Bluetooth samples in the training set, and each input IQ signal is projected before STFT or CWT representations are formed. The purpose is not to introduce another deep-learning architecture, but to examine whether geometrically grounded preprocessing can improve UAV classification under interference.

The main contributions of the paper are as follows. First, the paper formulates Null-Spacing for RF-UAV classification, where the removed subspace is estimated from Wi-Fi/Bluetooth references rather than from UAV data or arbitrary projection directions. Second, the effect of this preprocessing step is evaluated under a shared pipeline with STFT/CWT representations and two classifiers: a compact CNN and ResNet-18. This design allows the role of preprocessing to be separated from the downstream model. Third, the paper reports a held-out evaluation on CardRF under AWGN, Wi-Fi, Bluetooth, mixed-interference, and joint-negative SNR/SIR conditions, together with control projections and post-projection energy analysis to clarify when Null-Spacing helps and when it may fail.

2. RELATED WORK AND RESEARCH GAP

2.1. RF-based UAV classification under noise and interference

Studies on RF-based UAV classification generally follow two directions. One line of work relies on hand-crafted features such as RF fingerprints, frequency-domain descriptors, time-frequency features, and wavelet-based representations [2, 3, 7, 8]. These features are often easier to interpret because they are closely linked to signal-processing principles. However, their performance can drop when UAV emissions overlap with Wi-Fi, Bluetooth, or other RF sources in the observed band [3].

A second line of work relies on deep-learning models that learn representations directly from raw RF signals or from spectrograms [9-15]. Such models are able to capture more complex RF patterns than hand-crafted features. Their performance, however, still depends strongly on the input representation. If structured interference remains in the IQ signal, it will also appear in the spectrogram, together with UAV-related patterns.

Recent studies have considered noisy or interfered UAV/Flycam classification, for example by combining CNNs with constant false alarm rate (CFAR) filtering [21] or using compressive sensing and machine learning under Wi-Fi co-channel interference [22]. These works show that interference should be addressed directly in RF-UAV classification. However, in the surveyed studies, an IQ-domain preprocessing block based on Wi-Fi/Bluetooth-derived interference-subspace projection has not been separately evaluated.

2.2. RF signal representation for machine learning and deep learning

Input representation directly affects RF-based UAV classification. Previous studies have used RF fingerprints, frequency-domain features, wavelet features, and time-frequency spectrograms [2, 3, 8, 10, 14]. STFT is widely used because it converts IQ signals into two-dimensional spectrograms suitable for CNN-based classifiers. CWT provides an alternative multi-scale representation and is used in this paper as an additional configuration.

However, STFT and CWT mainly change the representation domain. They do not directly remove

interference from the IQ signal. When Wi-Fi or Bluetooth occupies a large part of the received energy, these components may remain visible in the classifier input. Therefore, this paper places Null-Spacing before STFT or CWT formation.

2.3. Subspace-based preprocessing and orthogonal projection

Subspace-based methods are widely used in signal processing to model or attenuate structured components in observed signals. In signal detection, a signal or interference component can be represented by a low-dimensional set of basis directions [16]. Orthogonal projection has also been used to remove unwanted components in data-processing problems such as hyperspectral image classification [17, 18].

In wireless systems, subspace projection has been studied for interference mitigation. For example, several works use orthogonal projection to attenuate interference in Global Navigation Satellite System (GNSS) receivers before subsequent acquisition, tracking, or navigation processing [19, 20]. The present work differs from GNSS anti-jamming in both objective and evaluation criterion. Here, projection is used as a preprocessing step for a downstream UAV classification task. Its usefulness is assessed by classification metrics and by the quality of the resulting time-frequency representation, rather than by signal recovery or navigation performance. In addition, the removed subspace is estimated from Wi-Fi/Bluetooth reference signals in the ISM band, not from a GNSS jamming model.

This idea is suitable for UAV classification in ISM bands because Wi-Fi and Bluetooth often have repeated emission patterns. Part of their energy may therefore concentrate along a limited number of dominant directions in the signal space. Once these directions are estimated from reference data, the observed IQ signal can be projected onto the orthogonal complement of the interference subspace. This step aims to attenuate structured interference before forming the classifier input representation.

2.4. Research gap and positioning of this paper

The reviewed literature shows that the main gap lies in the signal-processing stage before deep-learning representations are formed. Existing RF-UAV studies have explored many feature types and classifier architectures, but most of them handle noise and interference through feature engineering, spectrogram design, sampling mechanisms, or downstream models. In contrast, the IQ signal itself has rarely been treated as a separate preprocessing stage for attenuating structured interference before STFT or CWT is computed.

Although subspace projection has been studied in signal processing and interference mitigation, its use as a Wi-Fi/Bluetooth-derived IQ-domain preprocessing step for RF-UAV classification has not been separately evaluated in the surveyed literature. This paper addresses that gap by estimating an interference subspace from Wi-Fi/Bluetooth reference samples and applying Null-Spacing before forming the classifier input representation. The method does not replace the deep-learning classifier. Instead, it adds a geometrically grounded preprocessing step whose effect can be evaluated independently of the downstream model. The main question is whether this projection improves UAV classification in ISM bands, especially under low or negative SNR/SIR conditions.

3. PROPOSED METHOD

3.1. Signal model and proposed pipeline

We consider UAV classification from RF signals under a known class set $\mathcal{Y} = \{1,2,\dots,\mathrm{K}\}$, where K is the number of UAV classes. Each down-converted RF IQ window is written as $\mathbf{x} \in C^N$, with N IQ samples per window. In an ISM-band environment, the received vector is modeled as:

$$\mathbf{x} = \mathbf{s}_y + \mathbf{i} + \mathbf{n} \quad (1)$$

Here, $\mathbf{s}_y$ is the UAV signal associated with class y. The interference vector **i** includes structured RF emissions, mainly from Wi-Fi, Bluetooth, or other transmitters operating in the same band. The term **n** accounts for additive random noise.

The degradation level of an observation is described by two quantities: the signal-to-noise ratio (SNR) and the signal-to-interference ratio (SIR), defined as

$$\mathrm{SNR} = 10\log_{10}\frac{|\mathbf{s}_y|_2^2}{|\mathbf{n}|_2^2} \tag{2}$$

$$\mathrm{SIR} = 10\log_{10}\frac{|\mathbf{s}_y|_2^2}{|\mathbf{i}|_2^2} \tag{3}$$

When SNR < 0 dB or SIR < 0 dB, the UAV signal energy is lower than the corresponding noise or interference energy. In this case, discriminative information among UAV classes may be masked.

The classifier takes an IQ window as input and assigns it to one of the UAV classes, i.e.,

$$f_\theta: \mathbb{C}^N \to \mathcal{Y} \tag{4}$$

For a correctly classified sample, the predicted label $\hat{y}$ should match the true label y. In this work, the IQ signal is not classified in its original form. It is first processed by Null-Spacing and then transformed into a time-frequency representation before classification:

$$\mathbf{x} \xrightarrow{\mathbf{P}_\perp} \mathbf{x}_{NS} \xrightarrow{\mathcal{T}(\cdot)} \boldsymbol{X} \xrightarrow{g_\theta(\cdot)} \hat{y} \tag{5}$$

In (5), $\mathbf{P}_\perp$ denotes the projection onto the orthogonal complement of the estimated interference subspace, $\mathbf{x}_{NS}$ is the Null-Spacing output, $\mathcal{T}(\cdot)$ is the time-frequency representation transform, and $g_\theta(\cdot)$ is the classifier. In this study, $\mathcal{T}(\cdot)$ is implemented using the short-time Fourier transform or continuous wavelet transform. As illustrated in Figure 1, the proposed pipeline contains two stages: offline interference-subspace estimation and online Null-Spacing preprocessing followed by UAV classification.

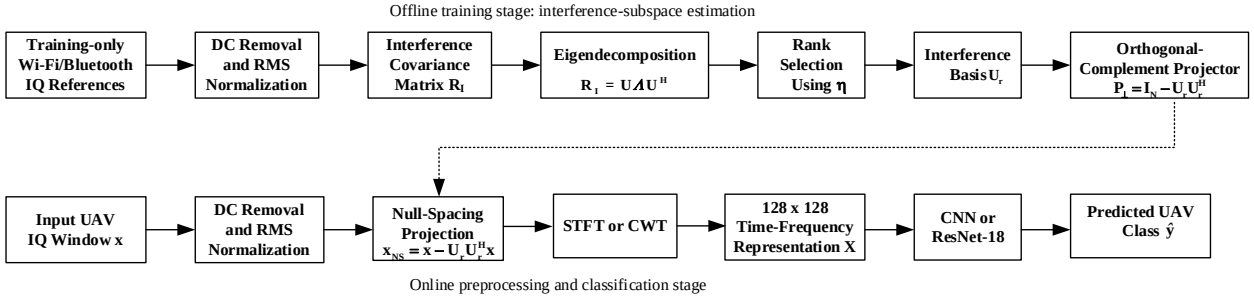


Figure 1: Offline estimation and online application of the proposed Null-Spacing pipeline.

In the offline stage, training-only Wi-Fi/Bluetooth IQ windows undergo direct-current (DC) removal and root-mean-square (RMS) normalization before covariance estimation and eigendecomposition. The leading eigenvectors selected by the cumulative-energy threshold η form the interference basis $\mathbf{U}_r$ and the projector $\mathbf{P}_\perp = \mathbf{I}_N - \mathbf{U}_r\mathbf{U}_r^H$. During validation and testing, this fixed projector attenuates the component of each normalized IQ window lying in the estimated interference subspace. The resulting signal is then converted into a 128 × 128 STFT or CWT representation and classified by the compact CNN or ResNet-18.

3.2. Estimation of the interference subspace

This paper assumes that, after power normalization, Wi-Fi/Bluetooth windows tend to concentrate their energy along a limited number of dominant directions in the signal space. These directions are estimated from the covariance matrix of a reference set and are used to approximate the interference subspace. This model is suitable for repeated structured interference, unlike white noise, which is not expected to concentrate along fixed directions.

Let the interference subspace be denoted by

$$\mathcal{U}_I = \mathrm{span}\{\mathbf{u}_1, \mathbf{u}_2, \ldots, \mathbf{u}_r\} \tag{6}$$

Here, r < N is the subspace dimension. The basis vectors are arranged as

$$\mathbf{U}_r = [\mathbf{u}_1, \mathbf{u}_2, \ldots, \mathbf{u}_r] \in C^{N\times r} \tag{7}$$

If the interference component **i** in (1) lies close to this subspace, it can be approximated as

$$\mathbf{i} \approx \mathbf{U}_{\mathrm{r}}\boldsymbol{\alpha} + \mathbf{e}_{\mathrm{I}} \tag{8}$$

The vector $\boldsymbol{\alpha} \in C^{\mathrm{r}}$ contains the representation coefficients in the interference-subspace basis. The component $\mathbf{e}_{\mathrm{I}}$ is the residual outside this subspace. When $||\mathbf{e}_{\mathrm{I}}||_2$ is small, the model indicates that most interference energy is concentrated in $\mathcal{U}_{\mathrm{I}}$.

To estimate $\mathcal{U}_{\mathrm{I}}$, an interference reference set is formed as

$$\mathcal{D}_{\mathrm{I}} = \{\mathbf{z}_1, \mathbf{z}_2, \ldots, \mathbf{z}_{\mathrm{M}}\} \tag{9}$$

This set contains signal windows $\mathrm{z_m} \in \mathrm{C^N}, \mathrm{m} = 1,2, \ldots, \mathrm{M}$, where each window is taken from Wi-Fi or Bluetooth signals without the target UAV signal. The reference set is taken only from the training split to avoid leakage into the test set. After power normalization, the sample covariance matrix is computed as

$$\mathbf{R}_{\mathrm{I}} = \frac{1}{\mathrm{M}} \sum_{\mathrm{m}=1}^{\mathrm{M}} \mathbf{z}_{\mathrm{m}} \mathbf{z}_{\mathrm{m}}^{\mathrm{H}} \tag{10}$$

The notation $(\cdot)^{\mathrm{H}}$ denotes the Hermitian transpose. The covariance matrix $\mathbf{R}_{\mathrm{I}}$ is then decomposed as

$$\mathbf{R}_{\mathrm{I}} = \mathbf{U}\boldsymbol{\Lambda}\mathbf{U}^{\mathrm{H}} \tag{11}$$

where

$$\boldsymbol{\Lambda} = \mathrm{diag}(\lambda_1, \lambda_2, \ldots, \lambda_{\mathrm{N}}), \quad \lambda_1 \geq \lambda_2 \geq \cdots \geq \lambda_{\mathrm{N}} \tag{12}$$

The eigenvectors associated with the r largest eigenvalues are selected to form $\mathbf{U}_{\mathrm{r}}$. When r is not set in advance, the interference-subspace dimension is determined by the cumulative energy threshold η:

$$r = \min\left\{q : \frac{\sum_{j=1}^{q} \lambda_j}{\sum_{j=1}^{N} \lambda_j} \geq \eta\right\} \tag{13}$$

This rule retains the dominant directions of the reference-interference energy. A larger η usually gives a larger r, which may remove more structured interference but can also increase the risk of attenuating UAV-related components. After $\mathbf{U}_{\mathrm{r}}$ is determined, the Null-Spacing projection is constructed to attenuate components lying in the interference subspace.

This construction assumes that the Wi-Fi/Bluetooth interference directions estimated from the training set remain representative for the test conditions. This is reasonable for the controlled CardRF evaluation, but may not hold in dynamic RF environments with different devices, channels, or traffic patterns. This motivates adaptive or multi-basis extensions of Null-Spacing.

3.3. Null-Spacing preprocessing

Null-Spacing projects the input signal onto the orthogonal complement of the interference subspace. Since $\mathbf{U}_{\mathrm{r}}$ is constructed from eigenvectors of the covariance matrix $\mathbf{R}_{\mathrm{I}}$, its columns are selected in orthonormal form:

$$\mathbf{U}_{\mathrm{r}}^{\mathrm{H}}\mathbf{U}_{\mathrm{r}} = \mathbf{I}_{\mathrm{r}} \tag{14}$$

Here, $\mathbf{I}_{\mathrm{r}}$ is the $r \times r$ identity matrix. The projection operator onto the interference subspace is

$$\mathbf{P}_{\mathrm{I}} = \mathbf{U}_{\mathrm{r}}\mathbf{U}_{\mathrm{r}}^{\mathrm{H}} \tag{15}$$

The projection operator onto the orthogonal complement of the interference subspace is then

$$\mathbf{P}_{\perp} = \mathbf{I}_{\mathrm{N}} - \mathbf{U}_{\mathrm{r}}\mathbf{U}_{\mathrm{r}}^{\mathrm{H}} \tag{16}$$

The matrix $\mathbf{I}_{\mathrm{N}}$ is the $N \times N$ identity matrix.

The signal after Null-Spacing preprocessing is

$$\mathbf{x}_{NS} = \mathbf{P}_{\perp}\mathbf{x} \tag{17}$$

Substituting the signal model in (1) into (17) gives

$$\mathbf{x}_{NS} = \mathbf{P}_{\perp}\mathbf{s}_{\mathrm{y}} + \mathbf{P}_{\perp}\mathbf{i} + \mathbf{P}_{\perp}\mathbf{n} \tag{18}$$

For the interference component represented in the interference subspace, projection onto the orthogonal complement removes this component because $\mathbf{P}_{\perp}\mathbf{U}_{\mathrm{r}} = 0$. Combining this property with the approximation in (8) gives

$$\mathbf{P}_{\perp}\mathbf{i} \approx \mathbf{P}_{\perp}\mathbf{e}_{\mathrm{I}} \tag{19}$$

Equation (19) shows that Null-Spacing attenuates the part of the interference modeled by the interference subspace. The remaining components include the projected UAV signal, the residual interference outside the subspace model, and the projected additive noise.

The projection affects not only the interference but also the UAV signal. The UAV signal can be

decomposed into two parts:

$$\mathbf{s}_{\mathrm{y}} = \mathbf{s}_{\mathrm{y},\parallel} + \mathbf{s}_{\mathrm{y},\perp} \tag{20}$$

These two components are defined as

$$\mathbf{s}_{\mathrm{y},\parallel} = \mathbf{P}_{\mathrm{I}}\mathbf{s}_{\mathrm{y}}, \quad \mathbf{s}_{\mathrm{y},\perp} = \mathbf{P}_{\perp}\mathbf{s}_{\mathrm{y}} \tag{21}$$

After Null-Spacing projection, only the component orthogonal to the interference subspace is retained:

$$\mathbf{P}_{\perp}\mathbf{s}_{\mathrm{y}} = \mathbf{s}_{\mathrm{y},\perp} \tag{22}$$

Thus, Null-Spacing does not preserve the entire UAV signal. The projection $\mathbf{P}_{\perp}$ removes components that lie in the interference subspace $\mathcal{U}_{\mathrm{I}}$. If the UAV signal also has a component lying in or near this subspace, that component will be attenuated together with the interference. Conversely, the UAV component orthogonal to $\mathcal{U}_{\mathrm{I}}$ is retained after projection. Therefore, Null-Spacing can improve performance when the interference is well modeled by $\mathcal{U}_{\mathrm{I}}$, but it may also remove part of the UAV information under clean conditions or when the UAV signal is very weak.

In practical implementation, it is not necessary to explicitly form the full matrix $\mathbf{P}_{\perp} \in C^{\mathrm{N}\times\mathrm{N}}$. With orthonormal $\mathbf{U}_{\mathrm{r}}$, the projected signal can be computed directly as

$$\mathbf{x}_{NS} = \mathbf{x} - \mathbf{U}_{\mathrm{r}}\mathbf{U}_{\mathrm{r}}^{\mathrm{H}}\mathbf{x} \tag{23}$$

This formula subtracts from the original signal its projection onto the interference directions in $\mathbf{U}_{\mathrm{r}}$. The main computational cost is approximately $\mathcal{O}(Nr)$ for each signal window. When $\mathrm{r} \ll \mathrm{N}$, this computation is less expensive than direct multiplication with the full projection matrix.

3.4. Signal representation and classifier

After Null-Spacing, the signal x_{NS} is converted into a representation for the classifier. The main configuration uses STFT. Let $\mathbf{x}_{\mathrm{NS}}[n]$ denote the *n*-th sample of the projected signal. The STFT is computed as:

$$\mathbf{S}[m,k] = \sum_{n=0}^{\mathrm{N}-1} \mathbf{x}_{\mathrm{NS}}[n]w[n-mH]\mathrm{e}^{-\mathrm{j}2\pi kn/L} \tag{24}$$

In (24), $w[\cdot]$ is the analysis window, H is the hop size, L is the FFT length, m is the time-frame index, and k is the frequency-bin index. The input spectrogram is computed in log-magnitude form:

$$\mathbf{X}[m,k] = 20\log_{10}(|\mathbf{S}[m,k]| + \epsilon) \tag{25}$$

The parameter ϵ is a small constant used to avoid taking the logarithm of zero. In addition to STFT, CWT is used as an additional configuration to examine the effect of Null-Spacing when the signal-representation domain is changed.

The deep-learning classifier is denoted by $g_{\theta}(\cdot)$. With the input representation $\boldsymbol{X}$, the model produces a probability distribution over K classes:

$$\mathbf{p} = g_{\theta}(\boldsymbol{X}), \qquad \mathbf{p} \in [0,1]^{\mathrm{K}}, \quad \sum_{\mathrm{k}=1}^{\mathrm{K}} \mathrm{p_k} = 1 \tag{26}$$

The predicted label is

$$\hat{y} = arg \max_{k\in\{1,\ldots,K\}} p_k \tag{27}$$

In the experiments, $g_{\theta}(\cdot)$ is either a compact CNN or a ResNet-18 adapted for single-channel spectrograms. In each comparison pair, the Raw branch and the Null-Spacing branch use the same classifier architecture. Therefore, the performance difference between the two branches mainly reflects the effect of preprocessing.

For a mini-batch of B samples, the cross-entropy loss is written as

$$\mathcal{L}_{\mathrm{CE}} = -\frac{1}{B}\sum_{b=1}^{B}\sum_{k=1}^{K} \mathbb{1}(y_b = k)\log p_{b,k} \tag{28}$$

Here, $p_{b,k}$ is the predicted probability of sample b for class k, and $\mathbb{1}(\cdot)$ is the indicator function.

4. EXPERIMENTS AND DISCUSSION OF RESULTS

4.1. Experimental setup

The experiments used the line-of-sight (LOS) portion of CardRF with five UAV classes:

BEEBEERUN, DJI_INSPIRE, DJI_M600, DJI_MAVICPRO, and DJI_PHANTOM [4]. Source files were separated before window extraction. The original LOS test partition was retained as an independent test set, while the LOS training partition was divided into class-stratified training and validation subsets at an 80:20 ratio using seed 20260425. The resulting UAV subsets contained 1,400, 350, and 750 source files for training, validation, and testing, respectively, corresponding to 280, 70, and 150 files per class.

Wi-Fi and Bluetooth files were also divided into mutually disjoint subsets. The interference basis was estimated only from the training-interference subset; training, validation, and test mixtures used interference files from their corresponding subsets. Therefore, no Wi-Fi or Bluetooth source used for subspace estimation was reused in validation or testing.

After DC removal and RMS normalization, four high-energy, non-overlapping windows of 8,192 complex samples were selected from each UAV file. Candidate starts were spaced by 4,096 samples, and selected starts were separated by at least 8,192 samples. The acquisition rate was 20 giga-samples per second (GSa/s). This procedure produced 5,600 training, 1,400 validation, and 3,000 test UAV windows. After generating one clean condition, six AWGN levels, six SIR levels for each of the Wi-Fi, Bluetooth, and mixed-interference scenarios, and nine joint-negative SNR/SIR combinations, the training, validation, and test sets contained 190,400, 47,600, and 102,000 samples, respectively. The AWGN SNR grid and the Wi-Fi, Bluetooth, and mixed-interference SIR grids were {-15, -10, -5, 0, 5, 10} dB. The joint-negative scenario used SNR, SIR ∈ {-15, -10, -5} dB, yielding nine combinations. These totals correspond to 38,080, 9,520, and 20,400 samples per UAV class in the training, validation, and test sets, respectively. Each test condition level or SNR/SIR combination contained 3,000 samples, including 600 samples per UAV class.

STFT used a 256-sample Hann window, a 256-point fast Fourier transform (FFT), 192-sample overlap, and 64-sample hop. The complex two-sided spectrum was frequency shifted, converted to log magnitude, normalized between its 1st and 99.5th percentiles, and resized to 128 × 128 pixels. For CWT, each window was resampled to 2,048 samples and transformed using 48 logarithmically spaced complex Morlet-like kernels with seven cycles and normalized center frequencies from 0.01 to 0.45 cycles/sample. The resulting scalogram was also resized to 128 × 128 pixels.

The compact CNN used four convolutional blocks with 16, 32, 64, and 128 channels, global adaptive average pooling, and dropout 0.25. ResNet-18 was trained from scratch with single-channel input and dropout 0.15. Both models used cross-entropy loss, AdamW, weight decay 10^{-4}, batch size 128, and at most 200 epochs. The initial learning rates were 10^{-3} for CNN and 5×10^{-4} for ResNet-18. The learning rate was reduced by a factor of 0.5 on a validation plateau, training stopped after 25 epochs without improvement in validation macro-F1, and the best validation checkpoint was evaluated on the test set. The main STFT + CNN comparison was repeated with five seeds from 20260425 to 20260429.

The evaluated configurations included $\eta \in \{0.95, 0.97, 0.99\}$, STFT + CNN, STFT + ResNet-18, CWT + CNN, random-subspace projection, UAV principal component analysis (UAV-PCA) subspace projection, Wiener filtering, and spectral subtraction. Accuracy and macro-F1 were reported, with macro-F1 used as the primary metric. Row-normalized confusion matrices and post-projection energy measures were also analyzed. The retained energy ratio is defined as:

$$\mathrm{R_{keep}} = \frac{\left|\left|\mathbf{x}_{NS}\right|\right|_2^2}{\left|\left|\mathbf{x}\right|\right|_2^2} \tag{29}$$

The removed energy ratio is defined as:

$$\mathrm{R_{remove}} = 1 - \mathrm{R_{keep}} \tag{30}$$

The retained energy level in dB is computed as:

$$\mathrm{E_{dB}} = 10 \log_{10} R_{\mathrm{keep}} \tag{31}$$

4.2. Overall results of the main configuration

The main configuration compares STFT + CNN without preprocessing against Null-Spacing ($\eta = 0.99$) + STFT + CNN on the same independent test set and using the same evaluation-scenario generation procedure. Table 1 reports the overall and condition-wise results.

Table 1: Overall results of the main configuration by test condition.

Condition	Raw Acc. (%)	Raw F1 (%)	Null-Spacing Acc. (%)	Null-Spacing F1 (%)	F1 gain (percentage points)
Clean	90.867	90.875	90.400	90.396	-0.479
AWGN	77.744	77.288	81.550	81.455	+4.167
Wi-Fi	89.739	89.748	89.661	89.698	-0.050
Bluetooth	89.367	89.402	89.889	89.898	+0.496
Mixed	88.000	88.016	89.206	89.251	+1.235
Joint-negative	73.378	72.851	76.070	75.811	+2.960
Overall	82.952	82.817	84.614	84.564	+1.747

Over the full test set, Null-Spacing increases accuracy from 82.952% to 84.614% and macro-F1 from 82.817% to 84.564%, a gain of 1.747 percentage points. The largest improvements occur under AWGN, mixed interference, and joint-negative conditions, whereas performance slightly decreases for clean signals and remains nearly unchanged for single-source Wi-Fi interference. Null-Spacing is therefore a conditional preprocessing step whose usefulness depends on the degradation condition and the UAV information retained after projection.

Table 2 shows the largest gain under negative-SNR AWGN, where macro-F1 increases by 9.165 percentage points. Gains of 2.708 and 2.957 points are obtained for difficult mixed-interference and joint-negative groups, respectively. However, at joint-negative SNR = -15 dB, macro-F1 decreases by 3.813 points, whereas it increases by 6.342 points at SNR = -10 and -5 dB. Thus, projection is beneficial only when sufficient discriminative UAV information remains.

Table 2: Macro-F1 results on difficult SNR/SIR groups for the main configuration.

Condition	Evaluation group	Raw F1 (%)	Null-Spacing F1 (%)	F1 gain (percentage points)
AWGN	SNR = -15, -10, -5 dB	68.156	77.321	+9.165
Wi-Fi	SIR = -15, -10 dB	88.137	88.534	+0.397
Bluetooth	SIR = -15, -10 dB	88.118	88.876	+0.758
Mixed	SIR = -15, -10 dB	84.508	87.216	+2.708
Joint-negative	All 9 negative combinations	72.826	75.783	+2.957
Joint-negative	SNR = -15 dB	67.925	64.112	-3.813
Joint-negative	SNR = -10, -5 dB	75.277	81.619	+6.342

Note: Grouped results are arithmetic means of the macro-F1 scores computed separately at each SNR/SIR level or combination. Therefore, they may differ slightly from the pooled scenario-level macro-F1 scores reported in Table 1.

4.3. Class-level analysis and post-projection energy level

Figure 2 compares the row-normalized confusion matrices under joint-negative SNR/SIR. Null-Spacing increases the correct classification rate of BEEBEERUN from 73.70% to 82.52% and that of DJI_INSPIRE from 39.78% to

52.20%; their F1 scores increase from 69.51% to 78.27% and from 44.46% to 55.10%, respectively.

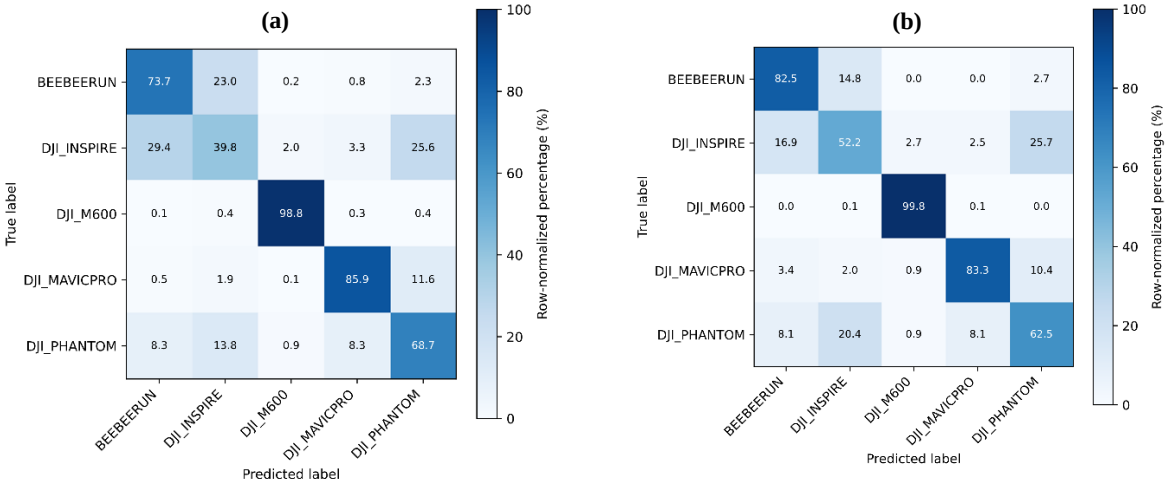


Figure 2: Row-normalized confusion matrices under the joint-negative condition.
(a) Raw STFT + CNN; (b) Null-Spacing η = 0.99 + STFT + CNN.

The effect remains class dependent. DJI_M600 is nearly unchanged, whereas DJI_MAVICPRO and DJI_PHANTOM slightly degrade. In particular, DJI_PHANTOM misclassification as DJI_INSPIRE increases from 13.83% to 20.43%, indicating possible loss of class-specific information after projection.

Table 3: Post-projection energy analysis by condition at η = 0.97 and η = 0.99.

η	r	Quantity	Clean	AWGN	Wi-Fi	Bluetooth	Mixed	Joint-negative
0.97	16	R_{keep} (%)	70.520	87.459	31.958	30.810	31.331	52.153
0.97	16	R_{remove} (%)	29.480	12.541	68.042	69.190	68.669	47.847
0.97	16	E_{dB}	-2.689	-0.777	-7.345	-7.923	-7.542	-3.477
0.99	30	R_{keep} (%)	64.252	84.720	27.755	27.637	27.658	50.993
0.99	30	R_{remove} (%)	35.748	15.280	72.245	72.363	72.342	49.007
0.99	30	E_{dB}	-3.763	-0.979	-9.058	-9.085	-9.010	-3.640

Tables 3 and 4 clarify this trade-off. At η = 0.99, Null-Spacing removes about 72% of the energy under Wi-Fi, Bluetooth, and mixed interference, but only 15.280% under AWGN, confirming that it is not a general white-noise filter. It also removes 35.748% under clean conditions. Class-wise, the removed clean-signal energy ranges from 0.799% for DJI_M600 to 75.780% for BEEBEERUN. Thus, performance improves when the removed energy mainly represents interference, but may decline when discriminative UAV components overlap with the estimated interference subspace.

Table 4: Class-wise energy analysis for clean UAV signals at η = 0.99.

UAV class	R_{keep} (%)	R_{remove} (%)	E_{dB}
BEEBEERUN	24.220	75.780	-11.089
DJI_INSPIRE	48.277	51.723	-3.985
DJI_M600	99.201	0.799	-0.035
DJI_MAVICPRO	87.961	12.039	-1.051
DJI_PHANTOM	61.600	38.400	-2.655

The values in Tables 3 and 4 are averages of sample-wise quantities. Owing to the nonlinear logarithmic transformation, the reported mean E_{dB} is not generally equal to $10\log_{10}$ of the reported mean R_{keep}.

4.4. Configuration comparison and stability evaluation

Table 5 extends the comparison to different signal representations and classifiers. In the STFT + CNN group, macro-F1 increases from 82.817% for the raw signal to 83.264%, 84.416%, and 84.564% at η = 0.95, η = 0.97, and η = 0.99, respectively. This result shows that η controls the effect of the projection. Together with Table 3, η can be viewed as a parameter that governs the trade-off between removing energy in the interference subspace and preserving useful UAV information. With CWT + CNN, Null-Spacing

also increases macro-F1 from 78.968% to 82.018%, indicating that the effect of projection is not limited to the STFT domain.

Table 5: Overall performance of experimental configurations.

Method	η	Accuracy (%)	Macro-F1 (%)
Raw STFT + CNN	-	82.952	82.817
Null-Spacing + STFT + CNN	0.95	83.363	83.264
Null-Spacing + STFT + CNN	0.97	84.550	84.416
Null-Spacing + STFT + CNN	0.99	84.614	84.564
Raw STFT + ResNet-18	-	85.910	85.783
Null-Spacing + STFT + ResNet-18	0.97	85.958	85.846
Null-Spacing + STFT + ResNet-18	0.99	86.017	85.987
Raw CWT + CNN	-	79.061	78.968
Null-Spacing + CWT + CNN	0.99	82.337	82.018
Random-subspace + STFT + CNN	0.99	82.775	82.387
UAV-PCA subspace + STFT + CNN	0.99	73.390	73.342

The smaller gain obtained with ResNet-18 indicates that a stronger classifier leaves less room for preprocessing improvement. The random-subspace and UAV-PCA controls achieve macro-F1 scores of 82.387% and 73.342%, respectively, confirming that the benefit does not arise from arbitrary dimensionality reduction.

Table 6: Comparison with preprocessing baselines in the STFT + CNN pipeline; condition-wise columns report macro-F1 (%), and Null-Spacing uses $\eta = 0.99$.

Method	Accuracy (%)	Macro-F1 (%)	Clean	AWGN	Wi-Fi	Bluetooth	Mixed	Joint-negative
Raw	82.952	82.817	90.875	77.288	89.748	89.402	88.016	72.851
Wiener filtering	80.144	79.753	90.369	69.331	88.804	88.607	87.368	68.463
Spectral subtraction	80.502	80.134	90.330	70.912	89.803	88.666	86.580	68.346
Null-Spacing	84.614	84.564	90.396	81.455	89.698	89.898	89.251	75.811

Table 6 shows that Null-Spacing achieves the highest overall macro-F1 of 84.564%, compared with 82.817% for no preprocessing, 79.753% for Wiener filtering, and 80.134% for spectral subtraction. Its advantage is largest under AWGN and joint-negative conditions, although the raw baseline remains slightly better for clean signals and spectral subtraction is marginally better for single-source Wi-Fi interference.

Table 7: Seed-stability comparison between Raw and Null-Spacing in the STFT + CNN pipeline.

Method	Number of seeds	Accuracy (%)	Macro-F1 (%)
Raw	5	82.795 ± 0.304	82.656 ± 0.275
Null-Spacing ($\eta = 0.99$)	5	84.651 ± 0.114	84.488 ± 0.118
Difference (Null-Spacing – Raw)	5 pairs	+1.856 ± 0.225	+1.832 ± 0.193

Table 7 summarizes the five-seed stability comparison between the Raw and Null-Spacing configurations in the STFT + CNN pipeline. Null-Spacing improves macro-F1 in all five paired runs, with an average gain of 1.832 ± 0.193 percentage points. The paired Wilcoxon signed-rank test yields $p = 0.03125$ for the one-sided test and $p = 0.0625$ for the two-sided test. Given the limited number of seeds, these results are interpreted as evidence of stability rather than as a comprehensive statistical significance analysis.

Scenario-wise analysis in Table 8 shows that the most stable gains are observed under additive white Gaussian noise, mixed interference, and joint-negative SNR/SIR conditions. Macro-F1 increases from 77.580 ± 0.335% to 81.429 ± 0.308%, from 87.770 ± 0.171% to 89.262 ± 0.068%, and from 72.866 ± 0.838% to 75.746 ± 0.292%, respectively. Under the clean-signal condition, the difference is almost zero, with 90.230 ± 0.518% compared with 90.259 ± 0.290%. This result is consistent with Sections 4.2 and 4.3, showing that Null-Spacing is more beneficial when the input signal is degraded by noise or structured interference.

Table 8: Scenario-wise seed-stability results in the STFT + CNN pipeline.

Scenario	Raw F1 (%)	Null-Spacing F1 (%)	F1 gain (percentage points)
Clean	90.230 ± 0.518	90.259 ± 0.290	+0.029
AWGN	77.580 ± 0.335	81.429 ± 0.308	+3.849
Wi-Fi	89.297 ± 0.254	89.753 ± 0.114	+0.456
Bluetooth	89.086 ± 0.220	89.604 ± 0.236	+0.518
Mixed	87.770 ± 0.171	89.262 ± 0.068	+1.492
Joint-negative	72.866 ± 0.838	75.746 ± 0.292	+2.880

4.5. Computational cost and limitations

Table 9 reports in-memory graphics processing unit (GPU) runtime at $\eta = 0.99$ on an NVIDIA RTX A3000 12 GB GPU. The benchmark used N = 8,192, r = 30, batch size 128, the same 256-point STFT configuration as the classification experiments, 20 warm-up iterations, and 100 timed repetitions. It includes normalization, projection, STFT, frequency shifting, log-magnitude conversion, percentile normalization, and resizing, but excludes disk input/output, host-to-device transfer, and classifier inference.

Table 9: In-memory GPU runtime of Null-Spacing and STFT representation formation at $\eta = 0.99$.

Test condition	Raw STFT representation (ms/window)	Null-Spacing projection (ms/window)	Null-Spacing + STFT representation (ms/window)	Added cost (ms/window)	Relative overhead (%)
Clean	0.078402	0.002043	0.079033	0.000631	0.80
Joint-negative	0.078572	0.002107	0.079416	0.000844	1.07
Average	0.078487	0.002075	0.079225	0.000738	0.94

Note: Added cost is the difference between the separately timed complete pipelines and may differ from the standalone projection time.

On average, Raw STFT requires 0.078487 ms/window, while Null-Spacing + STFT requires 0.079225 ms/window. The added cost is 0.000738 ms/window, or 0.94%, corresponding to approximately 12,622 windows/s. These measurements indicate limited preprocessing overhead but do not represent end-to-end deployment latency.

The main limitations are the fixed training-derived interference subspace, possible attenuation of UAV information, evaluation on only CardRF with controlled scenario generation, and runtime measurement on one GPU platform. Moreover, the five-seed analysis covers only the main configuration. Future work should consider adaptive subspace estimation, additional interference sources and datasets, naturally overlapped recordings, and edge hardware.

5. CONCLUSION

This paper evaluates Null-Spacing as an RF IQ-domain preprocessing step for UAV classification under ISM-band noise and interference. Using Wi-Fi/Bluetooth training references, the method estimates an interference subspace and projects each IQ window before STFT or CWT formation. With STFT + CNN at $\eta = 0.99$, accuracy increases from 82.952% to 84.614% and macro-F1 from 82.817% to 84.564%, with larger gains under negative-SNR AWGN, mixed interference, and joint-negative conditions. However, performance may decrease for clean inputs, extremely weak UAV signals, or classes whose discriminative components overlap with the interference subspace. Null-Spacing should therefore be regarded as a conditional preprocessing method rather than a universal RF filter.

REFERENCES

[1] B. Taha and A. Shoufan, Machine learning-based drone detection and classification: State-of-the-art in research, *IEEE Access*, vol. 7, pp. 138669–138682, 2019, doi: 10.1109/ACCESS.2019.2942944.

[2] M. Ezuma, F. Erden, C. K. Anjinappa, O. Ozdemir, and I. Guvenc, Micro-UAV detection and classification from RF fingerprints using machine learning techniques, in *Proc. IEEE Aerospace Conference*, 2019, pp. 1–13, doi: 10.1109/AERO.2019.8741970.

[3] M. Ezuma, F. Erden, C. K. Anjinappa, O. Ozdemir, and I. Guvenc, Detection and classification of UAVs using RF fingerprints in the presence of Wi-Fi and Bluetooth interference, *IEEE Open Journal of the Communications Society*, vol. 1, pp. 60–76, 2020, doi: 10.1109/OJCOMS.2019.2955889.
[4] O. O. Medaiyese, M. Ezuma, A. P. Lauf, and A. A. Adeniran, Cardinal RF (CardRF): An outdoor UAV/UAS/drone RF signals with Bluetooth and WiFi signals dataset, *IEEE DataPort*, 2022, doi: 10.21227/1XP7-GE95.
[5] R. Shi, X. Yu, S. Wang, Y. Zhang, L. Xu, P. Pan, and C. Ma, RFUAV: A benchmark dataset for unmanned aerial vehicle detection and identification, arXiv:2503.09033 [cs.RO], 2025, doi: 10.48550/arXiv.2503.09033.
[6] M. Rostami, A. Faysal, H. Xia, H. Kasasbeh, Z. Gao, and H. Wang, CageDroneRF: A large-scale RF benchmark and toolkit for drone perception, arXiv:2601.03302 [cs.CV], 2026, doi: 10.48550/arXiv.2601.03302.
[7] O. O. Medaiyese, M. Ezuma, A. P. Lauf, and A. A. Adeniran, Hierarchical learning framework for UAV detection and identification, *IEEE Journal of Radio Frequency Identification*, vol. 6, pp. 176–188, 2022, doi: 10.1109/JRFID.2022.3157653.
[8] O. O. Medaiyese, M. Ezuma, A. P. Lauf, and I. Guvenc, Wavelet transform analytics for RF-based UAV detection and identification system using machine learning, *Pervasive and Mobile Computing*, vol. 82, p. 101569, 2022, doi: 10.1016/j.pmcj.2022.101569.
[9] M. F. Al-Sa'd, A. Al-Ali, A. Mohamed, T. Khattab, and A. Erbad, RF-based drone detection and identification using deep learning approaches: An initiative towards a large open source drone database, *Future Generation Computer Systems*, vol. 100, pp. 86–97, 2019, doi: 10.1016/j.future.2019.05.007.
[10] E. Ozturk, F. Erden, and I. Guvenc, RF-based low-SNR classification of UAVs using convolutional neural networks, *ITU Journal on Future and Evolving Technologies*, vol. 2, no. 5, pp. 39–52, 2021, doi: 10.52953/QJGH3217.
[11] S. Basak, S. Rajendran, S. Pollin, and B. Scheers, Drone classification from RF fingerprints using deep residual nets, in *Proc. 2021 International Conference on COMmunication Systems and NETworkS (COMSNETS)*, 2021, pp. 548–555, doi: 10.1109/COMSNETS51098.2021.9352891.
[12] M. Zuo, S. Xie, X. Zhang, and M. Yang, Recognition of UAV video signal using RF fingerprints in the presence of WiFi interference, *IEEE Access*, vol. 9, pp. 88844–88851, 2021, doi: 10.1109/ACCESS.2021.3089590.
[13] S. S. Alam, A. Chakma, M. H. Rahman, R. B. Mofidul, M. M. Alam, I. B. K. Y. Utama, and Y. M. Jang, RF-enabled deep-learning-assisted drone detection and identification: An end-to-end approach, *Sensors*, vol. 23, no. 9, p. 4202, 2023, doi: 10.3390/s23094202.
[14] S. Glüge, M. Nyfeler, A. Aghaebrahimian, N. Ramagnano, and C. Schüpbach, Robust low-cost drone detection and classification using convolutional neural networks in low SNR environments, *IEEE Journal of Radio Frequency Identification*, vol. 8, pp. 821–830, 2024, doi: 10.1109/JRFID.2024.3487303.
[15] M. H. Rahman, J.-I. Baik, M. A. Aziz, R. Tabassum, M. A. S. Sejan, and H.-K. Song, Cascaded learning empowered classification of UAVs using radio frequency under wireless interference, *Alexandria Engineering Journal*, vol. 121, pp. 201–212, May 2025, doi: 10.1016/j.aej.2025.02.031.
[16] L. L. Scharf and B. Friedlander, Matched subspace detectors, *IEEE Transactions on Signal Processing*, vol. 42, no. 8, pp. 2146–2157, 1994, doi: 10.1109/78.301849.
[17] J. C. Harsanyi and C.-I. Chang, Hyperspectral image classification and dimensionality reduction: An orthogonal subspace projection approach, *IEEE Transactions on Geoscience and Remote Sensing*, vol. 32, no. 4, pp. 779–785, 1994, doi: 10.1109/36.298007.
[18] C.-I. Chang, Orthogonal subspace projection (OSP) revisited: A comprehensive study and analysis, *IEEE Transactions on Geoscience and Remote Sensing*, vol. 43, no. 3, pp. 502–518, 2005, doi: 10.1109/TGRS.2004.839543.
[19] L. Zhao, M. G. Amin, and A. R. Lindsey, GPS antijam via subspace projection: A performance analysis for FM interference in the C/A code, *Digital Signal Processing*, vol. 12, no. 2–3, pp. 175–192, 2002, doi: 10.1006/dspr.2002.0447.
[20] Y. Ren, Y. Zhi, H. Gao, and J. Zhang, Performance analysis of subspace projection algorithm with respect to projection length for GNSS jamming mitigation, *Digital Signal Processing*, vol. 142, p. 104212, 2023, doi: 10.1016/j.dsp.2023.104212.
[21] V. B. Nguyen, V. P. Hoang, V. S. Doan, X. T. Hoang, and D. L. Trinh, Application of CNN deep learning model and CFAR filtering technique for RF-based drone signal classification in noisy conditions, *Journal of Military Science and Technology*, vol. 96, no. 96, pp. 30–40, Jun. 2024, doi: 10.54939/1859-1043.j.mst.96.2024.30-40.
[22] V. K. Tran, A. T. Do, H. Q. Nguyen, and L. C. Nguyen, A proposed model for processing UAV signals in the presence of WiFi co-channel interference based on compressive sensing and machine learning, *Journal of Military Science and Technology*, no. 82, pp. 70–80, Oct. 2022, doi: 10.54939/1859-1043.j.mst.82.2022.70-80.

TIỀN XỬ LÝ NULL-SPACING CHO PHÂN LOẠI UAV TỪ TÍN HIỆU RF IQ TRONG MÔI TRƯỜNG CAN NHIỄU BĂNG ISM

NGUYỄN ĐĂNG HIẾU[1,2]*, NGUYỄN LÊ CƯỜNG[2], TRẦN VŨ KIÊN[2]
[1] *Học viện Kỹ thuật và Công nghệ an ninh; Việt Nam*
[2] *Trường Đại học Điện lực, Việt Nam*
* *Tác giả liên hệ: hieund@hvktcnan.edu.vn*

Tóm tắt. Phân loại phương tiện bay không người lái (UAV) từ tín hiệu tần số vô tuyến (RF) đồng pha/vuông pha (IQ) trong các băng công nghiệp, khoa học và y tế (ISM) thường bị suy giảm bởi nhiễu nền và can nhiễu đồng kênh. Bài báo này khảo sát Null-Spacing như một bước tiền xử lý trong miền IQ nhằm làm suy giảm can nhiễu có cấu trúc trước khi tạo biểu diễn bằng biến đổi Fourier thời gian ngắn (STFT) hoặc biến đổi wavelet liên tục (CWT). Không gian con can nhiễu được ước lượng từ các mẫu Wi-Fi/Bluetooth trong tập huấn luyện, và mỗi tín hiệu IQ được chiếu lên phần bù trực giao của không gian con này. Phương pháp được đánh giá trên bộ dữ liệu CardRF với năm lớp UAV trong các điều kiện nhiễu Gauss trắng cộng (AWGN), Wi-Fi, Bluetooth, can nhiễu hỗn hợp và tỷ số tín hiệu trên nhiễu (SNR)/tỷ số tín hiệu trên can nhiễu (SIR) đồng thời âm. Với cấu hình STFT + mạng nơ-ron tích chập (CNN) tại $\eta = 0,99$, Null-Spacing cải thiện macro-F1 từ 82,82% lên 84,56% và độ chính xác từ 82,95% lên 84,61%. Trong điều kiện AWGN với SNR âm, macro-F1 tăng 9,165 điểm phần trăm. Các thực nghiệm đối chứng cho thấy mức cải thiện không xuất phát từ phép chiếu tùy ý, mà từ không gian con can nhiễu được xây dựng từ các tín hiệu tham chiếu Wi-Fi/Bluetooth. Kết quả cho thấy Null-Spacing là một bước tiền xử lý có điều kiện: phương pháp tăng độ bền vững trong một số điều kiện nhiễu và can nhiễu khó, nhưng không mang lại lợi ích đồng đều trong mọi điều kiện tín hiệu.

Từ khóa: Phép biến đổi Wavelet liên tục, Không gian con nhiễu, Băng tần ISM, Khoảng cách điểm không, Phép chiếu vuông góc, Tín hiệu RF IQ, Phép biến đổi Fourier thời gian ngắn, Nhiễu có cấu trúc, Phân loại UAV.

Received on August 24 – 2026
Revised on October 08 – 2026